Universidad Carlos III de Madrid

Bachelor's Degree in Aerospace Engineering

Bachelor Thesis

EXPERIMENTAL VALIDATION OF RANS MODELS FOR COMPLEX SEPARATED FLOWS

Alejandro Güemes Jiménez

Supervised by:
Marco Raiola

Leganés, September 2015

Dedicated to
Chloé

Acknowledgements

First of all, I would like to thank my parents for their support during all these years, their patience, their unconditional love and for the education they have given me and has made me the person that I am today.

I want to thank my tutor Marco Raiola. His guidance during all my thesis work is priceless and I could not do this project without his continuous support, his patience, motivation, and immense knowledge.

Besides my tutor, I would like to thank Prof. Andrea Ianiro, Prof. Stefano Discetti, and Prof. Pablo Fajardo, for their continuous support during my thesis. They have helped me to locate and correct my mistakes, gaining experience and knowledge that will be of great help in my future projects.

I want to thank Carlos Cobos, the lab technician, for his help to prepare and carry out my experiments. I also place on record, my sense of gratitude to one and all, who directly or indirectly, have left their hand in this project.

Furthermore, I want to thank all my professors during the bachelor's degree, especially professors of the Aerospace engineering Department. All the knowledge I have applied to this project I have learnt principally of you.

Last but not the least, I would like to thank my closest classmates: four years ago we were a group of strangers, but today I can say that I could not have imagined this adventure without you.

To all of you, thank you.

Abstract

In a solar panel array, the first row of panels produces the separation of the flow, leading to a shielding effect. The shielding effect is a turbulent phenomenon. Computational Fluid Dynamics analysis represents a powerful tool for modelling fluid flow in turbulent conditions, but it is still severely challenged in scenarios with separated flows at relatively large Reynolds number.

The objective of this project is to demonstrate that the results obtained in a CFD analysis are reproduced in a wind tunnel test with the same conditions. The main measurement technique used in the experiments is Particle Image Velocimetry, which allows to obtain the mean velocity of the flow and its statistic turbulences. A steady Reynolds-Averaged Navier-Stokes model has been chose to carry out the CFD analysis.

The conclusions of the project are that RANS model works perfectly for the first separated flow, but it is necessary more experiments in order to know if it produces results at the separated flows of the last panels. The experience obtained from this project can help to improve the further analyses. Anyway, due to the unsteady character of the separated flow, URANS model should produce more accurate results.

Contents

List of Figures

List of Tables

Chapter 1

Introduction and object of study

The sun is a clean energy source, completely natural. The solar energy is not a threat to the environment like the fossil fuel or nuclear energy, and it does not generate greenhouse gases or pollution. The only impact that solar energy produces is from the chemicals and solvents needed to produce the photovoltaic cells of the solar panels. This is a small impact compared to what one oil spill can produce on the environment.

Solar energy can be converted into electricity or thermal energy. In both cases, it is necessary the use of solar panels where the solar collectors or photovoltaic cells are placed. Solar panels are placed on tracts of open land or building roofs that receive a large amount of light. To maximise the sunlight hours, solar panels are located in array form and can be orientated to the sun. Solar panels are designed to support the frontal wind, shielding effect is not taken into account.

In a solar panel array, the first row of panels deflects the frontal wind, causing a turbulent wake that impacts against the following panels. Due to shielding effect, the other rows may suffer of lighter average structural load, but are also likely to be subject to periodic forces generated in the wake. A deeper knowledge of the loads allows a reduction in maintenance costs and the price of the support structure production. This costs reduction will improve the competitive capacity of this type of energy, allowing a reduction in price.

Even if CFD analysis nowadays represents a powerful tool for modelling fluid flow in industrial applications, it is still severely challenged in scenarios like the one that is object of this study, i.e. separated flows at relatively large Reynolds number. The results of the CFD should be compared to experimental results, to make sure that the assumptions made in the CFD model are correct. In order to do this, an experimental campaign in a wind tunnel has been carried out on a simplified model of the solar array. The experimental results obtained in the wind tunnel are compared with a CFD model that simulates the same simplified model and conditions on the wind tunnel. Results on the real solar array would naturally differ from the ones of the experiment due to the impossibility to reproduce the real conditions for a real solar array in the wind tunnel test chamber.

The objective of this project is to demonstrate that the tendencies seen in the CFD analysis are reproduced in the wind tunnel testing, particularly in cases with high angle of attack (45°):

- high load at the first panel (incident flow);
- abrupt decrease of the load in the second panel;
- small increase at the third one;
- from there, the load decreases more slowly and asymptotically.

In order to get a validation for CFD analysis, the same panel array configuration and boundary conditions have been studied with both experimental measurements and computational simulation. Due to the limited dimensions of the test section, experiments has not been performed with a large

number of panel rows. Each panel has been equipped with pressure taps for pressure distribution along the chord of the panel itself. More details about experiment can be found in Chapter 4. The same panel configurations have been simulated with the CFD analysis, considering wind tunnel boundary conditions. In CFD simulation the hypothesis of two-dimensional flow has been assumed. In order to obtain the measurements, two different methods are used: Pitot tubes and Particle Image Velocimetry.

Chapter 2

Literature Review

2.1 Solar panels

2.1.1 Solar energy

One of the advantages of the solar energy is that it can produce two different types of energy: electrical and thermal. To produce electricity directly, photovoltaic cells are used. The sunlight, which is pure energy, impacts into the photovoltaic cells located in the surface of the solar panels. A built-in-potential barrier in the cell acts on these electrons to produce a voltage, which can be used to drive a current through a circuit. Guerrero-Lemus and Martínez-Duart (2012) say that in order to produce thermal energy, mirrors are used. They acts as optical elements to concentrate solar energy and converting it into thermal energy at medium and high temperatures. This thermal energy, usually carried by steam or hot air, is used to move turbines and, consequently, to produce electricity. There are four different concentrated solar power technologies if we attend to the mirror system:

1. Parabolic troughs
2. Parabolic dishes
3. Flat mirror, called heliostats, focused on a receptor located in a tower
4. Linear Fresnel reflectors, where no solar tracking is needed.

As it can be seen in the Figure 2.1, this project is relevant for the first and the fourth technologies, which are the ones that use solar panel arrays.

Apart from these two systems, solar panel arrays can be also used to heat up water inside them. This heated water can be used directly any required purpose or, as the Concentrated Solar Power, to move a turbine which produce electricity.

2.1.2 Solar panel loads

Shademan and Hangan (2010) concluded that for isolated panels the maximum force coefficients occur when the wind yaw angle is 0 or 180° depending upon clearance ratio[1]. Clearance ratio effects are complex, but significant. As it tends to zero, significant variations in force levels occur depending on the clearance ratio itself. In general, the negative downstream pressure is reduced by proximity to a ground plane since large scale turbulence fluctuations are suppressed. For the panel arrays, Chevalier and Norton (1979) found that the windward panel in the array absorbs less force than the equivalent isolated panel, so the subsequent panels receive loads which depend upon the

[1] Clearance ratio is the ratio between the chord of the panel and the distance from the lower part of the panel to the ground

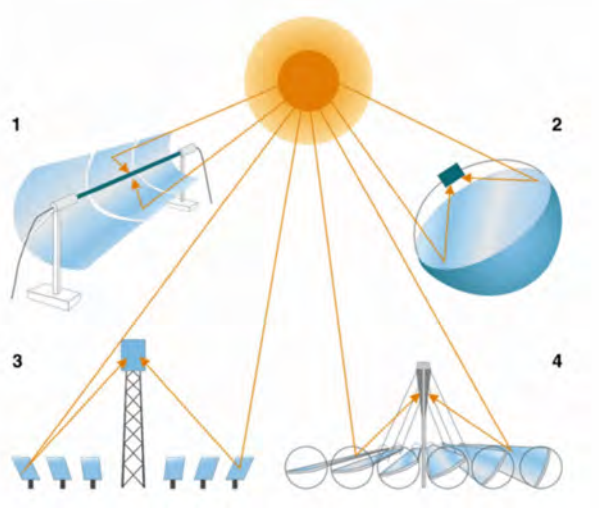

Figure 2.1: Solar energy types. Guerrero-Lemus and Martínez-Duart (2012)

pitch ratio[2].

There are models for isolated solar panel arrays that, when applied to multiple array configurations, do not produce the same results than in the experimental testing. In Chimney et al. (2012), a single solar panel array results showed that resultant forces and pressure values decrease highly at the first rows and tend to stabilise after a few rows. When the angle of inclination of the solar panels is increased, this decrease in forces along rows takes place faster. In Fajardo and Raiola (2014), it is seen that from the third row the force is proven to be less than 40% of the load on the first panel in both frontal and rear wind cases.

The wind can come from all the directions, so there are many cases of study changing the orientation of the solar panel arrays with respect to the air flow. Furthermore, solar panels can change their pitch in order to be more efficient catching the sunlight, so the studies like the one carried out by Shademan and Hangan (2010) also take into account this parameter.

Hosoya et al. (2008) state that Reynolds number similarity is required for both real and scaled solar panels. Since the dynamic viscosity μ of the air is equal for both, Reynolds number cannot be made equal with a reasonable wind velocity, because that velocity would introduce unacceptable compressibility effects. However, for sufficiently high Reynolds number ($> 2x10^4$) the pressure coefficient at any location on a blunt-sharp-edged body becomes independent of the Reynolds number.

Chevalier and Norton (1979) provides a CFD simulation with an experimental validation for flat plate type solar panels the azimuthal angle with respect to the wind direction and the inclination angle with respect to the horizon.

2.2 Turbulent flow

Capote et al. (2008) define the turbulence as the chaotic fluctuations of fluid dynamic quantities in space and time. This means that ,while in laminar flow the same conditions give us the same measurements (for example the same identical velocity in one point), in turbulent flow there will be a part that is fluctuating around a mean value (so measurements from one time to the other would differ). When turbulence appears, it usually dominates all other flow phenomena and results. Reynolds decomposition is introduced in order to simplify the Navier-Stokes problem.

[2]Pitch ratio is the ratio between the distance from the leading edge of the panel to the leading edge of the next panel and the distance from the lower part of the panel to the higher part

2.2.1 Navier-Stokes problem

The Navier-Stokes equations are the basic governing equations for a viscous, heat conducting fluid. They are a set of non-linear partial derivative equations that describe the fluid motion. They are obtained by applying Newton's laws of motion to each fluid element and are complemented by the continuity equation and the energy equation.

$$\frac{\partial \rho}{\partial t} + \frac{\partial}{\partial x_j}\left[\rho u_j\right] = 0 \tag{2.1}$$

$$\frac{\partial}{\partial t}\left(\rho u_i\right) + \frac{\partial}{\partial x_j}\left[\rho u_i u_j + p\delta_{ij} - \tau_{ji}\right] = 0 \tag{2.2}$$

$$\frac{\partial}{\partial t}\left(\rho e_0\right) + \frac{\partial}{\partial x_j}\left[\rho u_j e_0 + u_j p + q_j - u_i \tau_{ij}\right] = 0^3 \tag{2.3}$$

2.2.2 Reynolds number

Reynolds (1883) defines the Reynolds number as the ratio of inertial forces to viscous forces in a flow (see Equation 2.4). The inertial forces are defined as $\sim \frac{\rho U^2}{L}$, while the viscous forces are $\sim \frac{\mu U}{L^2}$,. It is used to determine if the fluid state is laminar or turbulent. Low Reynolds number stands for laminar flow and occurs when viscous forces are dominant, while the large ones do it for turbulent flow and occurs when the inertia forces are the dominant.

$$Re = \frac{\rho U L}{\mu} \tag{2.4}$$

2.2.3 Reynolds decomposition

Reynolds decomposition is the traditional method of decomposing a turbulent velocity field. One of its strengths is that it does a fair job of revealing the small-scale vortices, while its weaknesses is that it removes large-scale features mechanisms. The total velocityU^4 can be decomposed in two terms: the mean velocity $\bar{U}$ and the fluctuating term U'. Furthermore, the decomposed velocity can be steady or unsteady, as it can be seen in Figure 2.2.

$$U = \bar{U} + U' \tag{2.5}$$

The fluctuations are defined in such a way that their time average equals zero. Mathematically, the mean velocity is defined as:

$$\bar{U} = \lim_{T\to\infty} \frac{1}{T} \int_0^T U(x,t)dt \tag{2.6}$$

While the fluctuating term is defined by subtracting Equation 2.6 to U.

Use of Reynolds decomposition allows to rewrite the Navier-Stokes equations, obtaining a system of equations called Reynolds-Averaged Navier-Stokes equations (RANS). Quadrio (2012) describes the RANS equations as the equations primarily used to describe turbulent flows. They permit you not having to solve small scales of the problem, leading to faster computations than Navier-Stokes. When the Reynolds decomposition is input into the Navier-Stokes equation the closure problem appears: there are more unknowns than equations to solve. The RANS equations model the statistics ($\overline{u\prime_i u\prime_j}$) rather than physics ($u\prime_i, u\prime_j$), hiding small-scale interactions. The drawback is that sometimes the small details are important, like in combustion problems.

$$\rho\left[\frac{\partial \bar{u}_i}{\partial t} + \frac{\partial \bar{u}_j \bar{u}_i}{\partial x_j}\right] = \frac{\partial}{\partial x_j}\left(2\mu \bar{s}_{ji} - \rho\overline{u'_j u'_i}\right) - \frac{\partial \bar{p}}{\partial x_i} \tag{2.7}$$

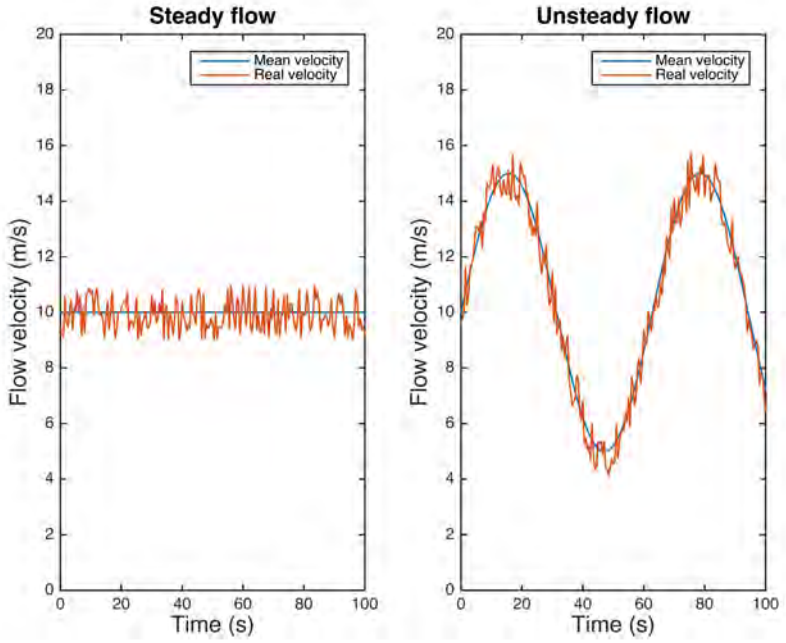

Figure 2.2: Reynolds decomposition for steady and unsteady flows

If the flow is unsteady, time averaging cannot be used and it must be replaced by ensemble averaging. This is done with Equation 2.8.

$$\bar{\phi}(x_i, t) = \lim_{N \to \infty} \frac{1}{N} \sum_{n=1}^{N} \phi(x_i, t) \tag{2.8}$$

2.2.4 Turbulence Kinetic Energy

The turbulence kinetic energy, k, is the kinetic energy per unit mass of the turbulent fluctuations in a turbulent flow. The SI unit of k is $J/kg = m^2/s^2$. It is characterised by measuring the root-mean-square (RMS) of the velocity fluctuations:

$$k = \frac{1}{2}(\langle u'u' \rangle + \langle v'v' \rangle + \langle w'w' \rangle) \tag{2.9}$$

Using the turbulence kinetic energy is possible to obtain the turbulence intensity I of the flow:

$$I = \frac{\sqrt{\frac{2}{3}k}}{U} \tag{2.10}$$

CFDOnline (2006) classifies turbulences depending on the turbulence intensity:

- High, if the turbulence intensity is between 5% and 20%
- Medium, if the turbulence intensity is between 1% and 5%
- Low, if the turbulence intensity is very low, well below 1%

[3]The total energy e_0 is defined by: $e_0 \equiv e + \frac{u_k u_k}{2}$
[4]U=u+v+w

2.2.5 Turbulence dissipation

Turbulence dissipation, ϵ, is defined as the rate at which turbulence kinetic energy is converted into thermal internal energy. The SI unit of ϵ is $J/(kg \cdot s)m^2/s^3$.

$$\epsilon = \nu \overline{\frac{\partial u_i'}{\partial x_k} \frac{\partial u_i'}{\partial x_k}} \tag{2.11}$$

2.2.6 Turbulence length scale

The turbulence length scale, l , is a physical measurement of the large eddies in a turbulent flow. The turbulent length scale is used to estimate the turbulent properties on the inlet boundary condition of a CFD simulation. In the $k - \epsilon$ model the turbulent length scale is computed as:

$$l = C_\mu \frac{k^{\frac{3}{2}}}{\epsilon}{}^5 \tag{2.12}$$

2.2.7 SST k-omega model

The Shear Stress Transport (SST) $k-\omega$ turbulence model is described for the first time in Menter (1993) and Menter (1994). It is composed by two-equation eddy-viscosity. The use of a $k - \omega$ formulation in the inner parts of the boundary layer allows to use the model directly in the wall through the viscous sub-layer, hence the SST $k - \omega$ model can be used as a low Reynolds turbulence model without any extra damping functions. The SST formulation also switches to a $k - \epsilon$ behaviour in the free-stream and thereby avoids the common $k - \omega$ problem that the model is too sensitive to the inlet free-stream turbulence properties. The SST $k - \omega$ model produces too large turbulence levels in zones with large normal strain, like stagnation zone or with strong acceleration. This tendency is much less pronounced than with a normal $k - \epsilon$ model though.

[5] C_μ is a model constant which in the standard version of the $k - \epsilon$ model has a value of 0.09.

Chapter 3

Measurement techniques

3.1 Particle Image Velocimetry

Particle Image Velocimetry (PIV) is an optical method of flow visualisation. The working principle of PIV is schematically described in Figure 3.1. According to Scarano and Westerweel (2008), PIV is based on the measurement of the displacement of small tracer particles that are carried by the fluid during a short time interval. These tracer particles are sufficiently small so that they accurately follow the streamlines along the fluid and do not alter the fluid properties or flow characteristics. The tracer particles are illuminated by means of a thin light sheet generated from a pulsed light source (usually a double-head pulsed laser system), and the light scattered by them is recorded onto two subsequent image frames by a digital imaging device. The particles recorded is these images look bigger than they are due to scattering. By means of stereoscopic imaging it is possible to determine the three components of the flow velocity within the planar field defined by the light sheet. PIV is essentially a non-intrusive measurement method, however it requires optical access for both the delivery of the light sheet and recording of the images. In order to obtain robust and unbiased measurements over the flow domain, it is important that the tracer particles are homogeneously distributed within the observed flow region.

The recorded images are typically processed off-line on a computer. Keane and Adrian (1992) explain that this consists essentially of a cross-correlation analysis of the particle-image patterns in small subdomains, or interrogation regions, between the first and second image frame.

An additional contribution of the PIV technique to experimental research is the capability to determine the flow velocity over a large number of points simultaneously, which allows a significant reduction of the time needed to acquire experimental data during in wind tunnel tests.

In Figure 3.2 and 3.3 it is possible to see how PIV images look like. The displayed images are saturated in order to make easier visualise the tracing particles.

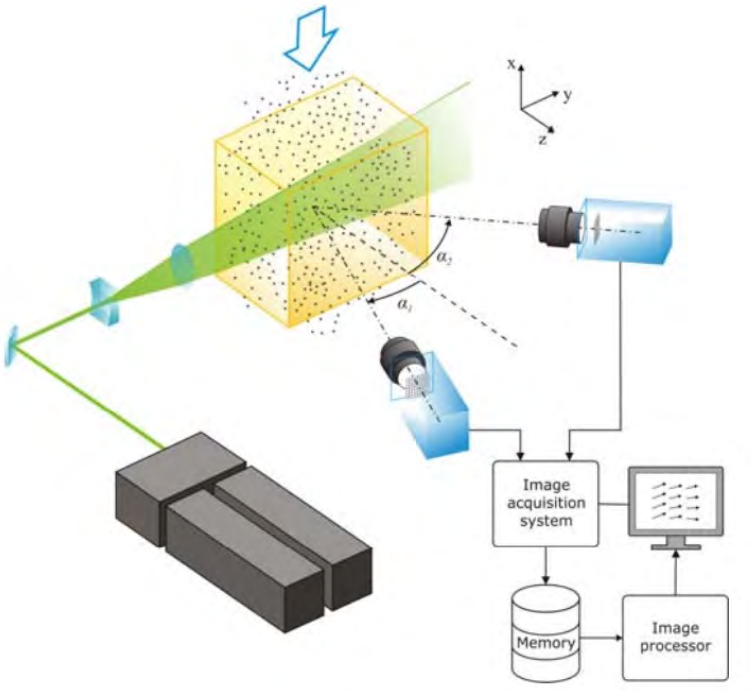

Figure 3.1: Schematic of a typical stereo-PIV measurement system. Scarano and Westerweel (2008)

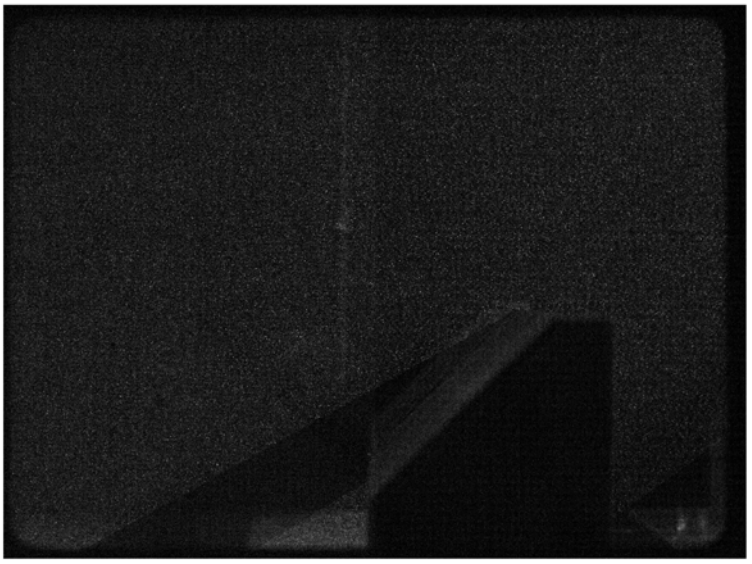

Figure 3.2: PIV image

Figure 3.3: PIV image

3.2 Pitot tube

The Bernouilli's equation seen in Equation 3.1 states that, along a streamline, the static pressure plus the dynamic pressure is equal to a constant, the total pressure.

$$p_{static} + \frac{1}{2}\rho v^2 = constant \tag{3.1}$$

The measured stagnation pressure cannot itself be used to determine the flow velocity. Velocity is measured from the dynamic pressure. The static pressure is measured with taps on the side surface of the tube (normal to stream direction). This is possible because in a boundary layer the pressure does not change in the normal-to-wall direction, so it is the same than in the free stream.

The dynamic pressure, then, is the difference between the stagnation pressure and the static pressure. The dynamic pressure is then determined using a diaphragm. If the air on one side of the diaphragm is at the static pressure, and the other at the stagnation pressure, then the deflection of the diaphragm is proportional to the dynamic pressure.

Pressure transducer measures the difference between two pressures. The first pressure corresponds to the fluid where the measurement is being taken, while the second one is the reference pressure. This reference pressure can be the perfect vacuum, leading to an absolute pressure measurement, or pressure in the measurement fluid, leading to a differential pressure. If the atmospheric pressure is used instead of the measurement fluid, the pressure transducer gives back a gauge pressure. There are different methods to perform the measurements:

- Force collector method measures strain due to applied pressure. There are different techniques to measure the strain, like the piezoresistive effect, piezoelectric effect, Hall effect, etc.
- Resonant method uses the changes in resonant frequency to measure stress, or changes in gas density, caused by applied pressure. This method is considered to provide very stable readings over time.
- Thermal method uses the changes in thermal conductivity of a gas due to density changes to measure pressure.
- Ionization method measures the flow of charged gas particles (ions) which varies due to density changes to measure pressure.

Pressure taps are small holes drilled perpendicular to the surface of the panel. Their purpose is to be a static pressure inlet for the pressure transducer. Pressure taps provide good results when they are small, sharp edged holes, perpendicular to a wall, which is parallel to a laminar flow. When the hole diameters are below 0.5 mm, it results in large response times and the holes are easily blocked by dust in the flow. In the other hand, large holes are less accurate by the amount of distortion they introduce in the flow field. Apart from this geometry criteria in order to have good results, there are other sources of measurement error like fluid turbulences, transonic and supersonic effects, the appearance of eddies developing inside the hole or the stagnation of the fluid in the hole.

Chapter 4

Experimental Setup

The experiment is designed to measure the velocity field and the turbulent statistics of the flow over a four-panel configuration. In order to do it, PIV method has been used. The laser of the PIV is located above the panels, with an angle of 45 degrees with respect to the horizontal plane to avoid reflections. The camera is located in front of the panels at the same height. It is possible for the camera to take a shot that covers all the panels, but the spatial resolution should be lowered, producing less accurate results, so camera obtains the images for each panel. This requires that the camera has to be moved and calibrated for each panel image.

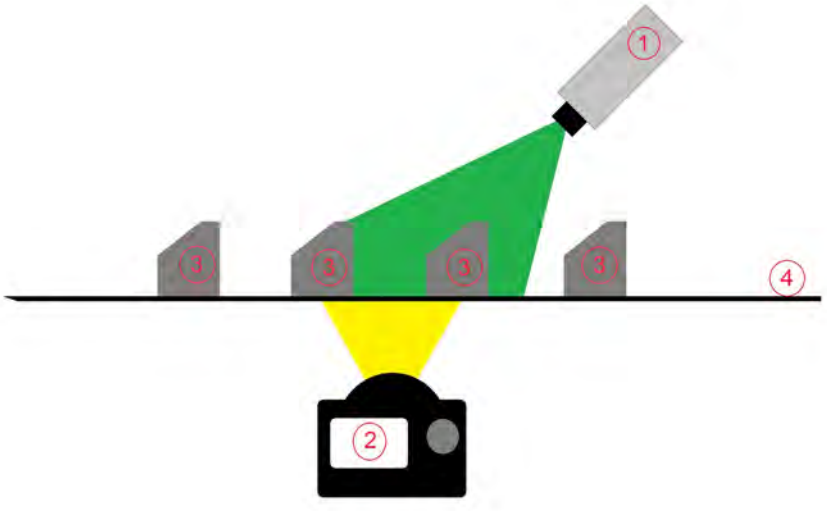

Figure 4.1: Experiment Sketch

Figure 4.1 shows a simplified sketch of the experiment where: 1) is the laser, 2) is the camera, 3) is the solar panels, and 4) is the splitter plate.

4.1 Models

The panels seen in Figure 4.2 should fulfil some requirements in order to simulate real solar panels. The designed panels should have a span of 400 mm, a chord length of 50 mm and a thickness of 5 mm. The center of the panel is expected to be at a distance of 0.75 chords from the ground. The

panel should form an angle of 45° with the ground.

Each panel is equipped with 6 pressure taps, 3 on the front side and 3 on the back side, close to the central section. On each side the pressure taps are positioned in the chord-wise direction at 25%, 50% and 75% of the chord. Front and back taps are displaced along the span-wise direction of 10 mm from the centre respectively on the left and on the right (the total distance between front and back taps is 20 mm). Each tap has initially a 1.2 mm diameter. The taps are connected to a pressure transducer through plastic measurement pipes.

If the panel were scaled to a real panel size, the thickness should be lower than 5 mm, but the measurement devices and the structural capabilities of the material do not allow it. It is that the reason why the thickness is 5 mm. The measurement pipes have a diameter of 1.2 mm and wall thickness should be at least 1 mm not to break. All this summed together is 3.2 mm, at which a safety factor has been applied to reduce the probability of failure.

In order to design the panels, SolidEdge V19 software has been used. The panel has been designed by pieces, trying to minimise the number of them that forms the panel. These pieces are designed in such a way to maximise the contact surface between them, in order to assure a good paste. Besides, the pieces must fulfil the maximum printing size allowed by the 3D printer. The model has been designed with 5 different types of pieces and formed by 8 pieces in total. In order to see more detailed explanation of the panel geometry, consult A. The assembly of the panels has been done using cyanoacrylate.

The panels have been manufactured in the 3D printer facility of Aerospace Engineering Group of Universidad Carlos III de Madrid. The printer is a Zcorp Zprinter 350 (Figure 4.3), capable of constructing a demonstration component with dimensions less than 203 x 254 x 203 mm on each side respectively with a resolution of 0.1 mm, utilising specially formulated gypsum (plaster of Paris) with an epoxy binder. In order to assembly the different parts, cyanoacrylate has been used. Cyanoacrylate is a strong fast-acting adhesive.

The pressure taps are connected to plastic pipes. The inner diameter of these pipes is 1.2 mm, but the outer diameter of the pipe is larger, so a drill is performed in each hole. The new diameter of the hole is large enough to allow pipes to pass without obstructing them but small enough to fasten the pipes. The pipes have enough length to pass them through all the wind tunnel and connect them to the pressure transducer. In this case this distance in 1.5 m.

As it will be explained coming shortly in Section 4.2.5, panels need to be painted in black to avoid reflections that can make PIV produce inaccurate results. To do this, a matte spray paint has been used.

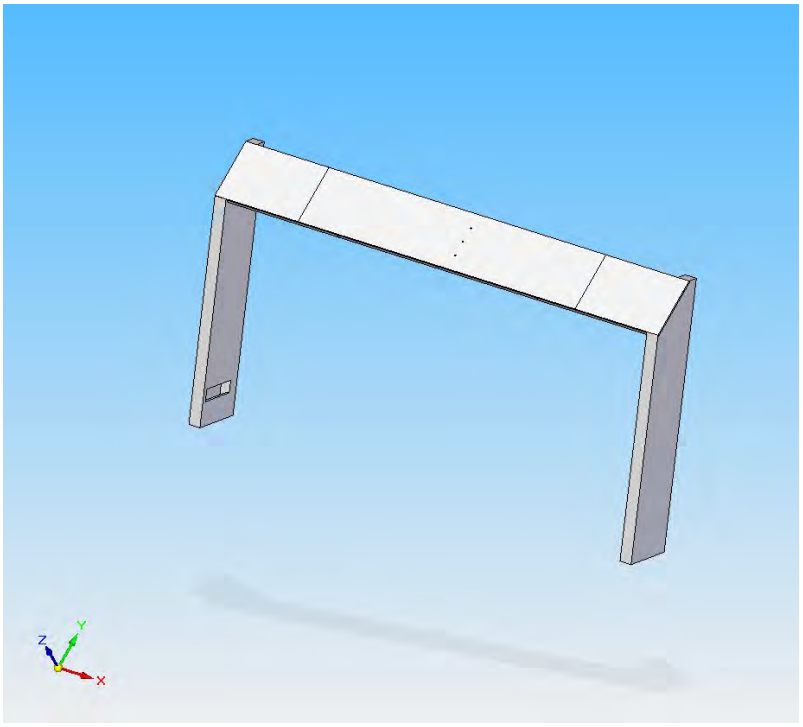

Figure 4.2: Panel model in Solid Edge V19

Figure 4.3: Zcorp Zprinter 350. © 3D Systems. All rights reserved

4.2 Equipment

All the equipments used in the experiment have been provided by Universidad Carlos III de Madrid.

4.2.1 Wind tunnel

To make the measurements, a recirculating wind tunnel is used. This tunnel belongs to the Department of Aerospace Engineering of the Universidad Carlos III de Madrid. The model of the tunnel is ARIES PXE2156. This tunnel is able to blow the air up to 20 m/s.

The tunnel is composed by different sections:

- Test chamber: section where the components to be tested are located. It consists of a cross section of 0.4 x 0.4m and a length of 1.5m. The transparent walls are made of Polymethylmethacrylate (PMMA). Access to the camera can be done by the both lateral walls, which are equipped with a full disassembling system.
- Fan system: The wind tunnel is equipped with four fans. While fans works some vibrations are produced that may cause a structural failure, so the fan system is equipped with dampers in each fan and between the structure and the fans system structure. The characteristics of the fans are shown in Table 4.1.
- Honeycomb: it removes swirl and lateral velocity variations and to make the flow more parallel to the axial axis.
- Diffuser: it is the gradually-expanding passage following the test section in which the flow speed decreases and the pressure rises.
- Convergent nozzle: it is used to accelerate the flow.

Installed power	0.25 kW
Maximum flow rate	5100
Level of maximum sound pressure	64 dB

Table 4.1: Wing tunnel data

The wind tunnel is controlled by a software provided by its manufacturer, so a computer is required. It is equipped with a honeycomb mesh. The honeycomb meshes are used as screens to get a uniform profile and to reduce the intensity of turbulence up to 1%. In the wind tunnel this is enough, but when a seeding source is added, turbulent structures created by the tracing particles might not be destroyed by the honeycomb, leading to an inlet turbulence intensity too high for a laminar flow.

4.2.2 Seeding

In order to visualise the flow motion with the PIV, tracer particle able to follow the streamlines of the fluid are needed. Furthermore, the quantity of particles should not saturate the flow in order to let light cover all the measuring zone. Achieving optimum flow seeding is generally acknowledged as the most difficult part of PIV experiments.

The seeding procedure consists of several steps. For air flows the seeding material needs first to be entrained in the working fluid and then inserted upstream of the measurement region. Devices that produce a mixture of air and seeding particles are commonly known as seeding generators. Generators of liquid droplets for air flows can be based on atomisers, Laskin nozzles or hot plate vaporisers/condenser (smoke machines). In this experiment, a Laskin nozzle is used fed with compressed air at 2 bar. A simplified sketch of Laskin nozzle can be seen in Figure 4.4:

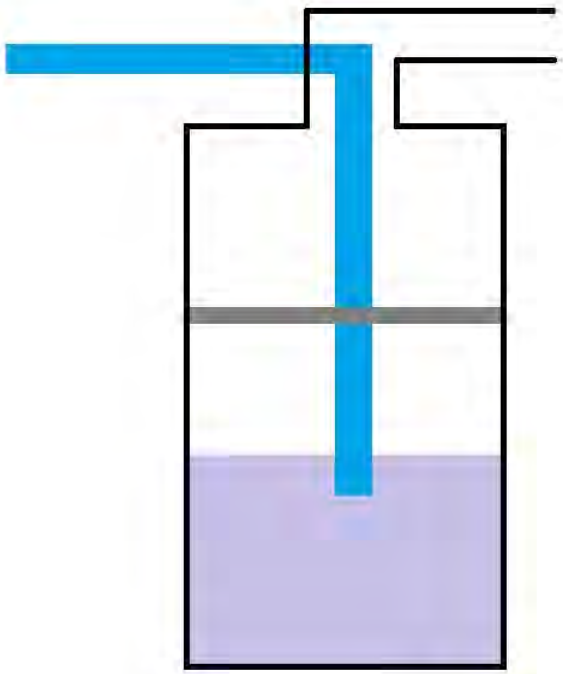

Figure 4.4: Laskin nozzle sketch

The seeding distribution system should not perturb the flow and at the same time should provide a homogeneous seeding level in the flow. This is usually accomplished with two-dimensional rakes of orifices placed upstream of screens and meshes in the wind tunnel settling chamber.

The Di-Ethyl-Hexyl-Sebacate ($C_{26}H_{50}O_4$) is the chosen seeding to perform the measurements. This choice was due to its favourable property not to be toxic if inhaled and easily evaporable in the air, so, in contrast with the others oils available, it leaves less residues and therefore the maintenance of the wind tunnel is considerably lower.

4.2.3 Splitter plate

A splitter plate has been used in order to simulate the ground inside the wind tunnel. Its objective is to divert the boundary layer created in the wind tunnel floor in order to provide a good flow to the panels. The splitter plate has a leading edge angle of 15°, and span width of 40 centimetres, the same than the wind tunnel.

4.2.4 Pressure transducer

The pressure transducer used to collect the data is Honeywell HSCSRRN001NDAA5.

HSC	High accuracy, compensated
S	Single inlet pin
RR	Dual radias barbed ports, same side
N	Dry gases, no diagnostics
001ND	Differential $\pm 1 in H_2O$
A	Analog
A	10% to 90% of V_{supply} (analog), 2^{14} counts (digital)
5	5.0 Vdc

Table 4.2: Pressure transducer data

4.2.5 Particle Image Velocimetry

Particle Image Velocimetry (PIV) is a method to provide an instantaneous velocity fields over 2D domains. Its principle is explained in Section 3.1. The PIV is composed by several elements that allow to make the measurements:

- an optically transparent medium seeded with tracer particles;
- a pulsed light source (laser) to illuminate the region of interest with a thin light sheet;
- a recording hardware;
- a computer with specific software to process the recorded images;
- a synchronizer to manage the illumination system and the recording camera.

The objects inside the region of interest should reflect as less light as possible in order to avoid erroneous measurements. Therefore, the panel surfaces and the board should be black, which is the colour that reflect less light.

The PIV system generates two light beams in sequence using the laser and capture the images with the camera. In the experiment, there is only one camera available, so it is placed along the normal axis of the light plane in order to obtain the velocity field in the illuminated plane (2D).

To obtain the two light beams, a Big Sky Laser CFR400 has been used. This laser needs some time to charge again for the next shoot. This charging time exceeds the Δt required between each pair of images. Due to this, the pulsed light source used counts with two independent lasers, reducing the delay time. The current technological limit for the time separation of each laser head is approximately 1/15s.

Due to its workings characteristics, the laser needs to be cool down in order to maintain its working temperature. The cooler (Figure 4.6) is provided together the power supply in a single compact, portable unit. The cooling system is automatically powered up when the system prime power turned on. Coolant interlocks prevent laser operation without coolant flow and during overtemperature conditions. The coolant motor pumps coolant to the pump cavity at greater than

Figure 4.5: Big Sky Laser CFR400

0.25 gallons per minute. A flow interlock switch ensures proper coolant flow and prevents damage, keeping the flow rate below this level. A temperature interlock on the heat exchanger senses the coolant temperature, and in the event of an over-temperature condition shuts the laser down. These safety features prevent catastrophic damage to the laser head. The 473 mL reservoir capacity is sufficient, when coupled to the 250 watt liquid-to-air heat exchanger, to properly cool the laser. All materials in the coolant loop have been selected to be compatible with the coolant and pump cavity to ensure reliability and long life. Heat distilled water with resistivity of 1Mohm-cm to 5Mohm-cm is the only coolant recommended. A flowchart of the cooling process can be seen in Figure 4.7.

In the experiment, a TSI Power View Plus 2MP camera (Figure 4.8) has been used. This camera has a pixels resolution of 1600 x 1200 and the sensor size is 74 x 7.4. To ensure that camera, laser and acquisition workstation are coordinated a synchroniser must be incorporated in the system.

In order to estimate the flow field, a cross-correlation between the two particles distributions is performed. Each frame is divided in smaller sectors and the cross-correlation peak provides then the most likely displacement of that set of particles. The time between the two captured images (Δt) is obtained by measuring the airspeed in the wind tunnel and the number of pixel that the particles must cover in the image. This Δt must be small enough to avoid particles to escape from the image.

Figure 4.6: Laser cooler

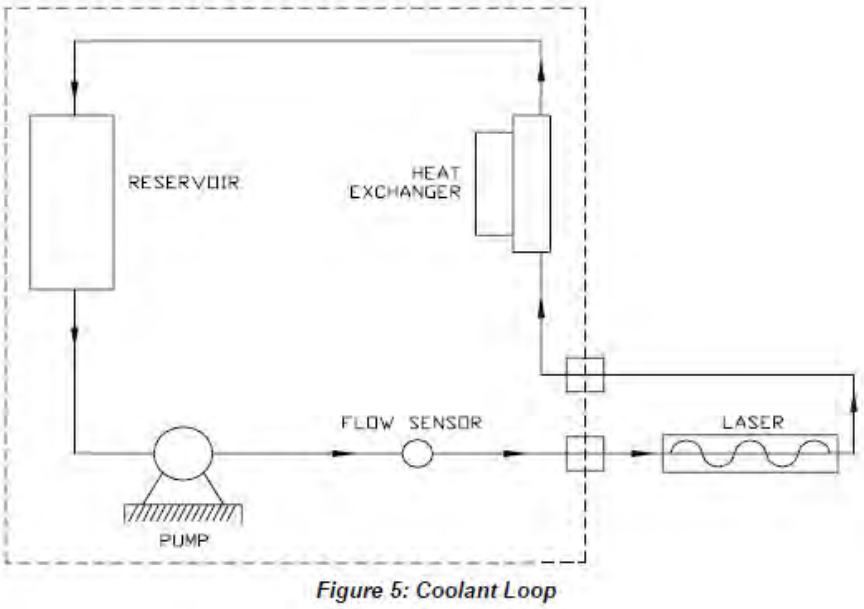

Figure 4.7: Cooling process

4.2.6 Experimental uncertainties

Due to evaporation, the concentration of tracing particle decreases during the images recording, making necessary to add more particles at the middle of the experiment. This causes that some images are not suitable to obtain accurate results for both too low or too high particle concentration, because it is not possible to make the cross-correlation between images.

Figure 4.8: TSI Power View Plus 2MP camera

PIV is supposed to take photos when the tracing particle are enlighten by the laser. Unfortunately, some elements inside the test section reflect the laser light, hiding particles from the camera in some zones. Furthermore, reflections can easily be stronger than the particles and moreover cover a wider zone, leading to saturate the pixels of the CCD and burn them. The measurements obtained in those zones are unrealistic, and they must not be taken into account. The objects that are sensitive to produce reflections are the edges of the panels and the panel surfaces where the black paint has some defects. During the experiments, the reflection provoked by the paint has been removed by painting the conflictive surfaces with a black marker pen, but the reflections provoked by the edges have been impossible. In order to solve this problem, the adopted solution has been to cut off the light beam that impacted on the edges. It has been localised the inlet point of the light beam in the ceiling and covered with an opaque surface. This leads to a shaded zone where the particles are not illuminated, so the measurement that the PIV provides in this regions should not be taken into account. In any case, the zone that cannot be taken into account after covering the edges is much smaller than the zone affected by the reflections.

The free stream velocity and the air temperature are measured before starting the image acquisition period, so due to any instabilities inside the wind tunnel they may vary slightly during the experiments. In addition, before collecting the free stream velocity and the air temperature, the wind tunnel must be self-stabilised. The stabilisation requires a large timeout period and it has been observed that the temperature has problem to be fixed, so it is another source of uncertainty during the experiments.

4.2.7 Safety precautions

In order to make the experiments in a safety environment, some precautions have been taken. This is completely necessary, because an experiment that threatens the health is not acceptable by any academic institution or company.

Manufacturing process

During the manufacturing process, some activities has been realised in a room with good ventilation. These activities are the extraction of the different panel pieces from the printer and the painting process of those pieces. When the pieces are extracted they are inside a cube full of powder that has to be removed. The printer allows to do it inside the printing section with a vacuum cleaner, but there are a lot of particle that goes into the air. With respect to the printing process, the paint used can be toxic if it is inhaled during a long period.

As it is explained in Section 4.1, the panels are pasted using cyanoacrylate, a fast-acting adhesive, so when it enters in contact with the skin it sticks. To avoid this, special gloves have been used, which protect the skin from the adhesive and allows to keep working. In addition, the cyanoacrylate has a minor toxicity, so when it evaporates it may enter in contact with the eyes and irritate them. To avoid it, a chemical extractor and glasses have been used.

Experiments

The laser used for the PIV method is very dangerous. When the laser is used at high power, it can make a person blind if the light beam impacts directly into the eyes. To avoid this, special glasses have been used. This glasses do not allow the light beam to pass, keeping the eyes safe.

4.2.8 Image processing

Before applying the PIV software to the set of images, they are pre-processed. Xu et al. (2006) define the eigenbackground subtraction as a commonly used method for moving object detection in the computer vision field. The method uses the difference between an input image and the reconstructed background image for detecting foreground objects based on eigenvalue decomposition. It takes the set of images and makes a Singular Value Decomposition (SVD). SVD arranges the eigenvalues from the largest to the smallest, or, in other words, arranging them based on the variance of the eigenimage. This basically depends on the spatial and temporal coherence of the eigenimage. In the PIV, the background has the maximum coherence, so it is placed in the first modes, while the particles have very low coherence. Using this technique, it is possible to remove the modes associated with the background, removing the reflections that may vary in the time.

The next step is to applied the PIV algorithm. It is written in C language and must be run in Windows OS. The output of the program is a set of .plt files, which are vector-based plotter files, corresponding to each pair of images and a .plt file corresponding to the statistics of the measurements.

The .plt files can be read using a MATLAB code. First, the file that contain the measurement statistics is printed, but the turbulence statistics results does not show any coherence with expected results. To solve this problem, the set of .plt images has been filtered out to eliminate all those images whose signal noise is greater than 0.3.

Masking

As it is explained in Section 4.2.6, in the measurements there are zones that should not be taken into account because they are shaded to avoid reflection. Furthermore, the measurements taken in front of the lateral part of the panels are not valid, because the measurements taken there do not correspond to the middle section of the panels but to the lateral supports. In order to provide a better understanding of the results to a person who has not participated in the experiment, the mask seen in Figure 4.9 is applied to the results to show only the zones where the measurements are reliable.

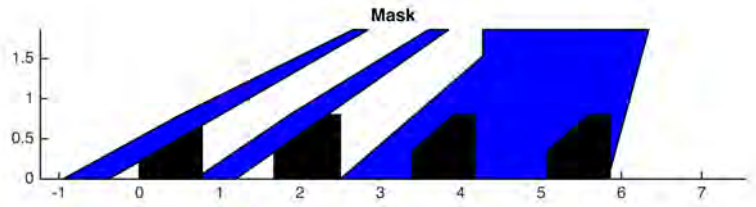

Figure 4.9: Mask

Chapter 5

Numerical setup

The Navier-Stokes equations that govern flow and heat transfer do not used to have analytical solutions, except for very simple cases. Fluent is a CFD software, developed by Ansys, which allows to solve fluid problems. In our case of study, the FLUENT case has been defined as the area zone between the split plate and the ceiling of the wind tunnel, and between the leading edge of the split plate and far away from the fourth panel, in order to analyse a fully developed wake.

5.1 Mesh

In order to save time and money, a good mesh is important. When the mesh is the source of wrong results is because of:

- Mesh too coarse.
- High skewness.
- Large jumps in volume between adjacent cells.
- Large aspect ratios.
- Inappropriate boundary layer mesh.

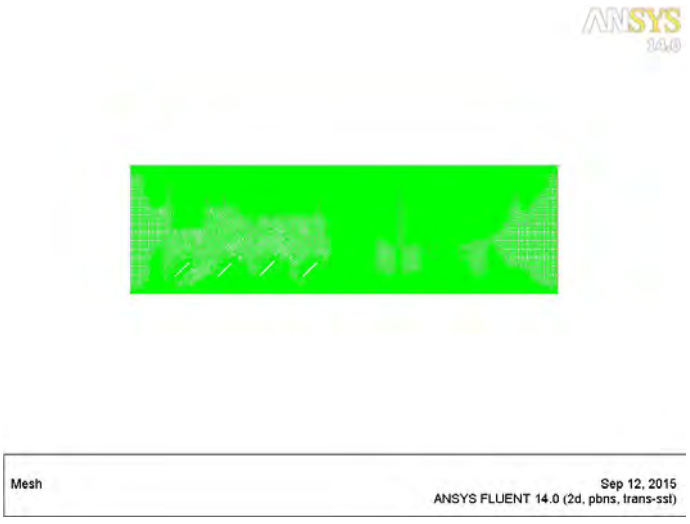

Figure 5.1: Mesh

The problem geometry is meshed with a minimum face element of 0.001 m and a maximum one of 0.003 m. The mesh is set to be structured with quadrilateral cells, but as the geometry

cannot be fully discretised in quadrilaterals, there is also triangular cells. There are some important zone where more accurate calculations are required, like the surrounding zones of the panels. In these zones, it has been set a fixed face value of 0.001 m. An example can be seen in Figure 5.2. Furthermore, the floor and ceiling walls has been also sized with a face value of 0.001 m to take into account the boundary layer separation in these zones. Finally, the mesh used for the calculations has nodes.

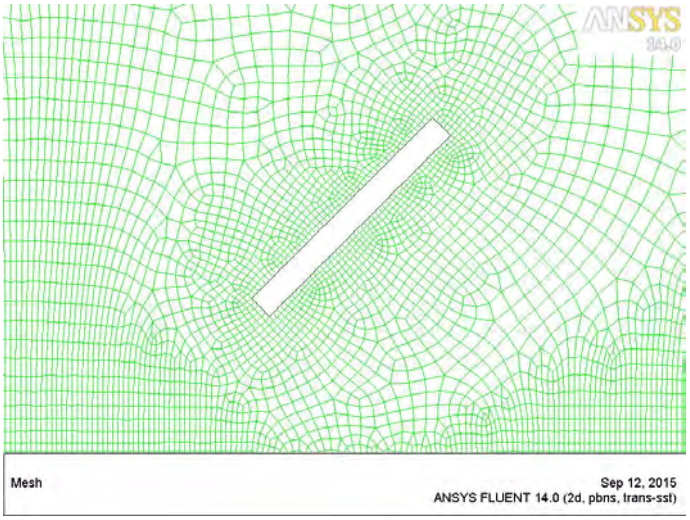

Figure 5.2: Mesh detail

5.2 Turbulence model

The transition SST model is based on the coupling of the SST k-omega transport equations shown in Section 2.2.7 with two other transport equations, one for the intermittency and one for the transition onset criteria, in terms of momentum-thickness Reynolds number. The SST model does not use wall functions and tends to be most accurate when solving the flow near walls. Furthermore, the solution is not always converged quickly, so the k-epsilon or k-omega models are often solved first to give good initial conditions. Menter et al. (2006) have develop an empirical correlation used by FLUENT software, which allows to cover the standard bypass transition as well as flows in low free-stream turbulence environments. The transition-SST model has some characteristics that should be taken into account. The turbulence intensity specified at an inlet can decay quite rapidly depending on the inlet viscosity ratio (the larger the inlet viscosity ratio, the smaller the turbulent decay rate). When viscosity ratio defined as inlet condition is too large, the skin friction can deviate significantly from the laminar value. This effect has been demonstrated experimentally that occurs, but nowadays it has not been possible to show how the transition SST model reproduces this behaviour in an accurate way. This makes desirable to set the inlet viscosity condition at a relatively low value and to estimate the inlet value of turbulence intensity. This model is described in Equation 5.1, Equation5.2, Equation 5.3, Equation 5.4 and Equation 5.5:

$$\frac{\partial}{\partial t}(\rho k) + \frac{\partial}{\partial x_j}(\rho u_j k) = \tilde{P}_k - \tilde{D}_k + \frac{\partial}{\partial x_j}\left((\mu + \sigma_k \mu_t)\frac{\partial k}{\partial x_j}\right) \tag{5.1}$$

$$\tilde{P}_k = \gamma_{eff} P_k \tag{5.2}$$

$$\tilde{D}_k = min(max(\gamma_{eff}, 0.1), 1.0) D_k \tag{5.3}$$

$$R_y = \frac{\rho y \sqrt{k}}{\mu} \tag{5.4}$$

$$F_3 = e^{-}\left(\frac{R_y}{120}\right)^3 \tag{5.5}$$

where P_k and D_k are the original production and destruction terms for the SST model and F_{1orig} is the original SST blending function. Note that the production term in the omega-equation is not modified.

5.3 Boundary conditions

5.3.1 Inlet

The inlet zone requires to define the inlet velocity as well as the temperature. Both of the them have been selected from the mean value of the data recorded before starting each experiment and shown in Table 6.1. Furthermore, FLUENT requires to define the turbulence length scale. It has been set at 0.05 m, because the chord length of the panels is 0.05 m.

In Section 5.2, it is said that the initial value of the turbulence intensity has to be estimated, but the data obtained in the experiments are available. The inlet turbulence intensity value has been set as follows: a line perpendicular to the inlet flow stream and upstream of the panels has been selected, with the values of the turbulence intensity present in this line a mean average has been computed, but not taking into account the corner values because there may appear unrealistic values due to the PIV capabilities. Looking properly at Figure 5.3, it can be seen that the turbulence intensity value taken from the PIV is recorded at one chord before the first panel, while the inlet zone of the FLUENT case is located 2 chords before the first panel. This has been done by assuming that the flow measured with the PIV faraway enough of the first panel is laminar, so

it is expected to maintain the value upstream.

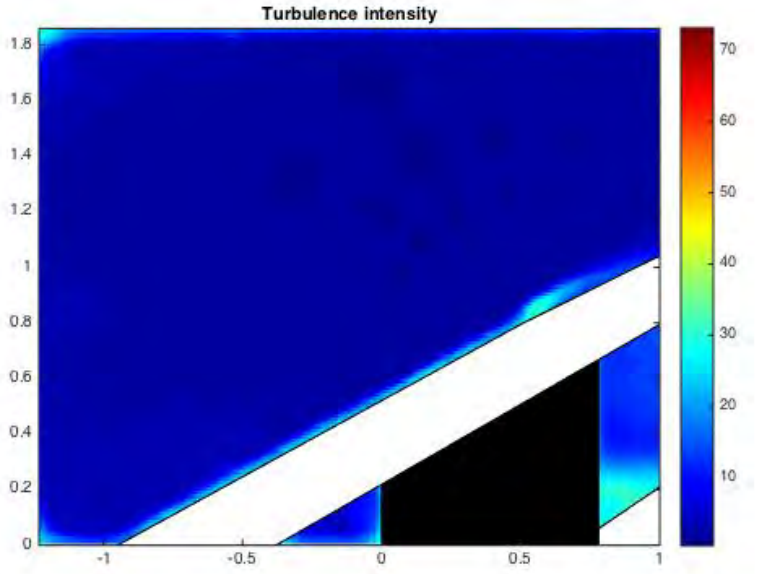

Figure 5.3: Turbulence intensity measurement at the inlet section

5.3.2 Outlet

The outlet zone has been defined as a pressured outlet. FLUENT requires to defined a gauge pressure. It is assumed that the ambient pressure in the outlet of the test section is the same than the pressure in the inlet. The pressure values were recorded before starting each experiment and are shown in Table 6.1. Taking all this into account, the gauge pressure at the outlet has been set at zero Pascals.

5.3.3 Floor, ceiling, and panels

The floor, ceiling and panels have been defined as walls in the boundary conditions. The walls have been defined as stationary walls and with no heat flux.

5.4 Solution method

The chosen method to solve the FLUENT case is the SIMPLEC (Semi-Implicit Method for Pressure Linked Equations-Consistent) algorithm. SIMPLEC algorithm is a variation of the SIMPLE algorithm and it is supposed to converge between 1.2 and 1.3 times faster.

The SIMPLE algorithm is iterative. Before solving the equations, it sets the boundary conditions and compute the velocity and pressure gradient. With this data, it solves the discretized momentum equations and the pressure correction equation (see Equation 5.6). Before finishing, it does some corrections in the face mass fluxes and cell velocities.

$$\frac{\delta}{\delta x_i}\left[\frac{\rho}{A_P^{u_i}}\left(\frac{\delta p'}{\delta x_i}\right)\right]_P = \left[\frac{\delta\left(\rho u_i^{m*}\right)}{\delta x_i}\right]_P + \left[\frac{\delta\left(\rho \tilde{u}_i'\right)}{\delta x_i}\right] \tag{5.6}$$

$$F_t = max(F_{1orig}, F_3) \tag{5.7}$$

Chapter 6

Results

6.1 Experimental data

As the experiment is recorded to keep a good spatial resolution, four different shooting have been done. The first shooting records the particle before the first panel, the second shooting between the first panel and the second, the third shooting between the second panel and the third, and the fourth shooting after the fourth panel. It is not possible to record images between the third and fourth panel, as it is explained in Section 4.2.6.

	Temperature ($°C$)	Pressure (Pa)	Velocity (m/s)	Reynolds number
Shooting 1	32.33	102100	12.7746	39740.597
Shooting 2	32.43	102100	12.8785	40040.773
Shooting 3	32.63	101900	12.8036	39684.093
Shooting 4	31.32	101600	12.7746	39777.831

Table 6.1: Experimental conditions

The Reynolds numbers have been calculated using the chord length of the panels as the parameter L of Equation 2.4. In order to obtain the pressure taps measurements, LabView software has been used.

6.2 Analysis of results

Before starting to analyse the results, they have been dimensionless. The spatial coordinates have been divided by the chord of the panels, while the velocity measurements have been divided by the free stream velocity U_∞ and the turbulence kinetic energy measurements have been divided by the velocity squared U_∞^2.

6.2.1 Comparison of velocity U_x

Figure 6.1 and Figure 6.2 show the mean velocity of the fluid in the x-direction. Comparing both images, it can be seen that, in front of the first panel ($x/c = 0$), both the experimental and the numerical results show a bubble where the velocity drops up to $0.5U_\infty$, due to the impact of the free-stream flow against the first panel.

If the fluid that leaves the panel at the top is compared, it can be seen that the velocity is increased up to $1.5U_\infty$, following the same pattern in both experimental and numerical results.

Figure 6.1 does not show all the region between first and second panel, but the visible region is enough to be compared with the region in Figure 6.2. Both of them show a region with velocity

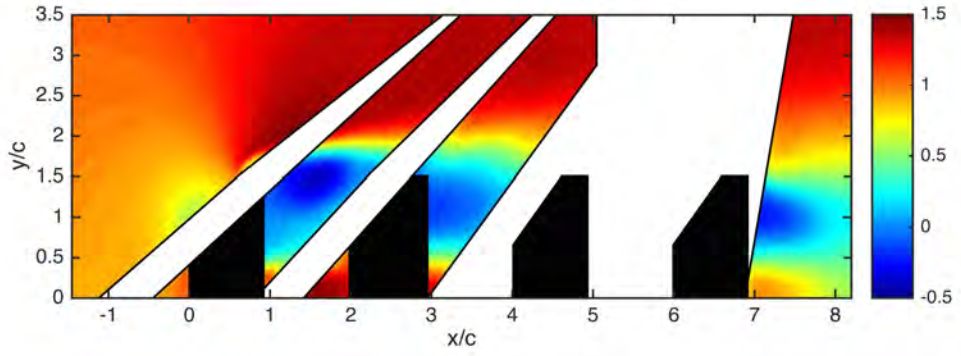

Figure 6.1: U_x obtained from the experimental results

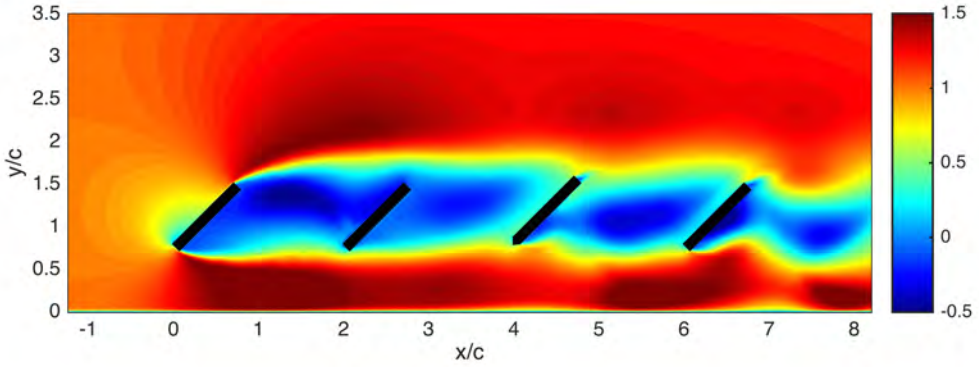

Figure 6.2: U_x obtained from the numerical results

of $-0.5U_\infty$. The same behaviour occurs between the second and the third panel, but in this case the maximum reversible velocity is lower, $-0.25U_\infty$.

When the region after the fourth panel is compared, it can be seen that both experimental and numerical results show a reversible flow, but the pattern described by the flow is not the same.

Figure 6.1 does not show much region of the flow above the splitter plate. Looking at the visible triangle before $x/c = 2$, it can be seen a region of accelerated flow up to $1.5U_\infty$, which accord with what appears in Figure 6.2.

6.2.2 Comparison of velocity U_y

Figure 6.3 and Figure 6.4 show the mean velocity of the fluid in the y-direction. Comparing both images, it can be seen that in the inlet section, both the experimental and the numerical results show a region with no vertical velocity. This is expected as long as the free stream provided by the wind tunnel has a good quality.

Looking at Figure 6.3, it can be seen that above the first panel the free stream increases it velocity in the y-direction. The fluid goes primarily up because, due to the angle of the panels with respect to the splitter plate, it is easier to go up without reverse the flow direction in the x-axis. It creates a pattern that looks like a bubble and one very similar can be found in Figure 6.4. The highest peak is $0.8U_\infty$ and appears at the top edge of the panel.

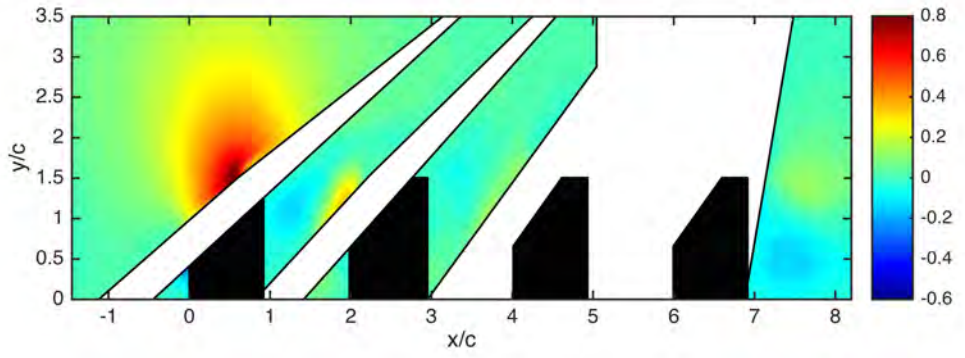

Figure 6.3: U_y obtained from the experimental results

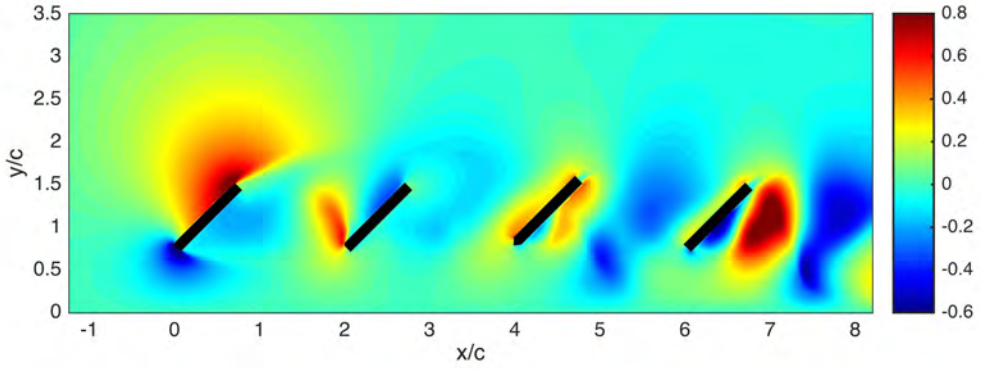

Figure 6.4: U_y obtained from the numerical results

6.2.3 Comparison of Turbulent Kinetic Energy

Figure 6.5 and Figure 6.6 show the experimental and numerical turbulence kinetic energy. Before facing the first panel, it can be seen in both figure that the turbulence kinetic energy does not suffer any change, maintaining a low level, because the flow has not been disturbed by any surface.

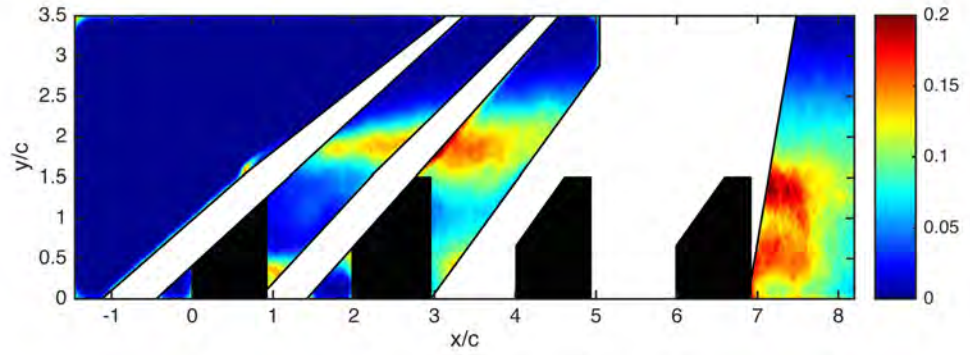

Figure 6.5: Turbulence Kinetic Energy obtained from the experimental results

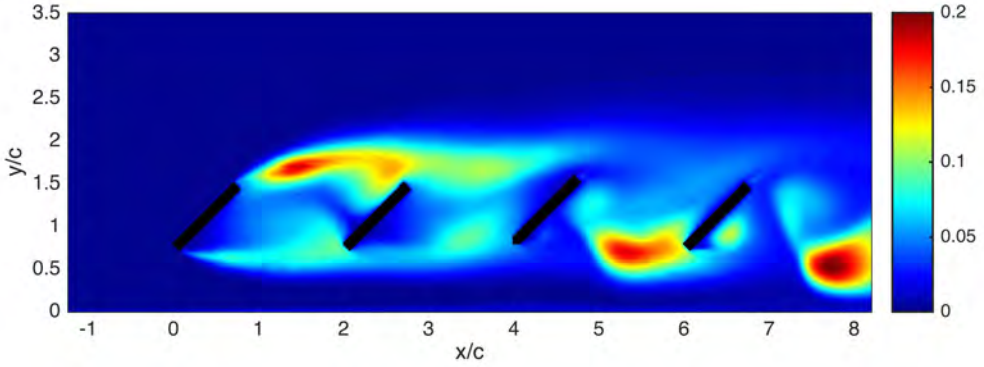

Figure 6.6: Turbulence Kinetic Energy obtained from the numerical results

When the flow reaches the first panel, $x/c = 0$, the flow detaches the panel at both top and bottom edges. This creates a turbulence wake at each edge with high turbulence kinetic energy. Figure 6.5 shows better the top wake than the bottom one due to the masking, and it shows similarity with the numerical results of Figure 6.6. However, the magnitude of the experimental result is $0.13U_\infty^2$, lower than the numerical prediction of $0.2U_\infty^2$. In the experimental result there is not much visibility of the bottom zone after the first panel, but it can be seen a small region right after the first panel where the turbulence kinetic energy increases up to $0.12U_\infty^2$. This turbulence kinetic energy is larger than the numerical result shows.

After the second panel, $x/c = 2$, the experimental results keeps showing the detached wake, but it has increased its size and the magnitude of the turbulence kinetic energy, reaching a value of $0.175U_\infty^2$. However, the numerical result does not show the same behaviour. The turbulence

wake is still existing, but it does not increase its size, while the magnitude of the turbulence kinetic energy is decreased to a value of $0.1U_{\infty}^2$.

In the experimental result, after the fourth panel it can be seen two wakes with high turbulence kinetic energy from $x/c = 7$ up to $x/c = 7.6$, where they start to decrease. However, the numerical simulation does not show this result, but a wake of high turbulence kinetic energy at the bottom region after the fourth panel.

6.2.4 Comparison of Turbulence Intensity

The turbulence intensity measured with the PIV at the inlet of the wind tunnel ($x/c = -1$ and $y/c = 1.5$) is 2.54%. It is calculated using Equation 2.9, but the PIV does not allow to measure w velocity. In order to solve the problem, it has been assumed that $\langle w'w' \rangle = \frac{1}{2}(\langle u'u' \rangle + \langle v'v' \rangle)$.

The turbulence intensity is based on the turbulence kinetic energy, so the pattern shown in both results should be equal. This can be checked by comparing Figure 6.5 with Figure 6.7 and Figure 6.6 with Figure 6.8. Unfortunately, this means that while at the first panels the experimental results shows resemblance with the numerical simulation, it does not coincide at the fourth panel.

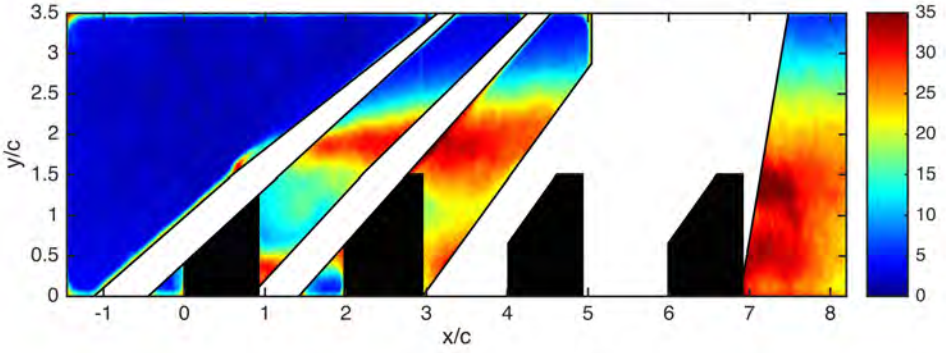

Figure 6.7: Turbulence Intensity obtained from the experimental results

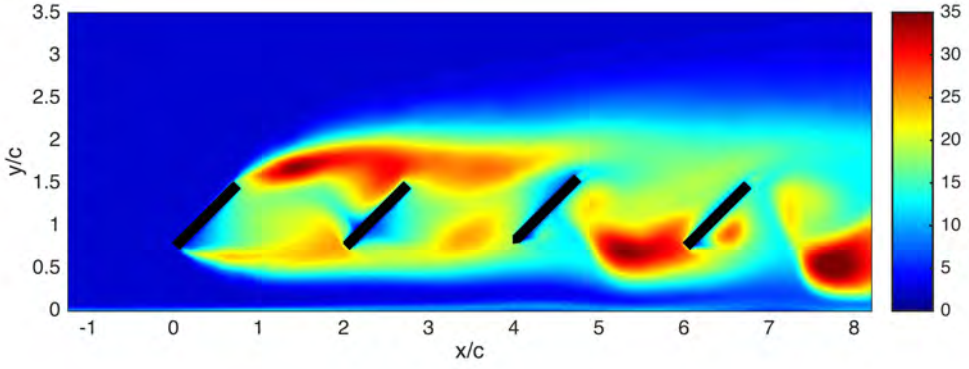

Figure 6.8: Turbulence Intensity obtained from the numerical results

6.2.5 Pressure Taps

The pressure taps equipped in the solar panels measure the static pressure on them with respect to a reference static pressure. This reference static pressure is the static pressure inside the tunnel. The relative static pressure from the experiments are compared with the distribution of the static pressure obtained from FLUENT. The FLUENT static pressure is a gauge pressure, that is relative to a pre-defined operating (static) pressure. As it is explained in Section 4.1, the solar panels are equipped with 6 pressure taps, 3 in the front and 3 in the back of the panel.

Before analysing the results, it must be taken into account that the experimental and numerical results do not have the same reference static pressure. This happens because there is not direct measurement of the static pressure inside the tunnel, so it have been recorded a reference value. This reference static pressure has been used for the numerical simulations, but it is not the real one used in the experiments.

Furthermore, during the pressure data collection it has been observed that the measurements are not steady in two taps of the second and fourth panels. The contamination of the tubes connecting the pressure taps with the pressure transducer may produce this behaviour. The seeding particles may have penetrated in the tubes clogging them, which can produce unrealistic results. Clogging can also occur due to water condensation inside tubes. However, it has to be taken into account that RANS is steady.

With respect to the simulation, there are also sources of possible errors. The mesh used is coarse and it does not have a very good quality, although it is acceptable. In addition, an unsteady problem is modelled with a steady simulation, which can leads to unrealistic results.

Figure 6.9 shows the relative static pressure for the first panel. It can be seen that the maximum relative static pressure is produced in the front side, at 25% of the panel chord, and it decreased along the chord. On the back side, the pressure taps records a constant relative static pressure along all the chord. All this behaviour fits with numerical simulation obtained from FLUENT.

Figure 6.10 shows the relative static pressure for the second panel. In the front side, the wind tunnel measurements show a constant relative static pressure. In the back side, the relative static pressure increases along the panel chord. However, the wind tunnel measurements do not fit perfectly with the FLUENT results. The front side pressure is also constant, but the back side pressure does not increase as in the experimental results. The maximum relative static pressure occurs at the front side.

Figure 6.11 shows the relative static pressure for the third panel. The experimental relative static pressure is constant in the front panel along the chord. This also happens in the back side of the panel, but with a lower value. However, in numerical results the largest pressure peak appears at the back side of the panel, at $x/c = 0.05$. Furthermore, the relative static pressure is not constant.

Figure 6.12 shows the relative static pressure for the fourth panel. The experimental results show a relative static pressure that has a large drop between $x/c = 0.25$ and $x/c = 0.5$ and then increases slightly. However, when the experimental results are compared with the numerical ones they do not fit perfectly. The measurements at the back side agree with the numerical simulation, but this numerical simulation a relative static pressure that increases slightly in the front panel. As it is explained above, this resuts may appear due to the tubes contamination.

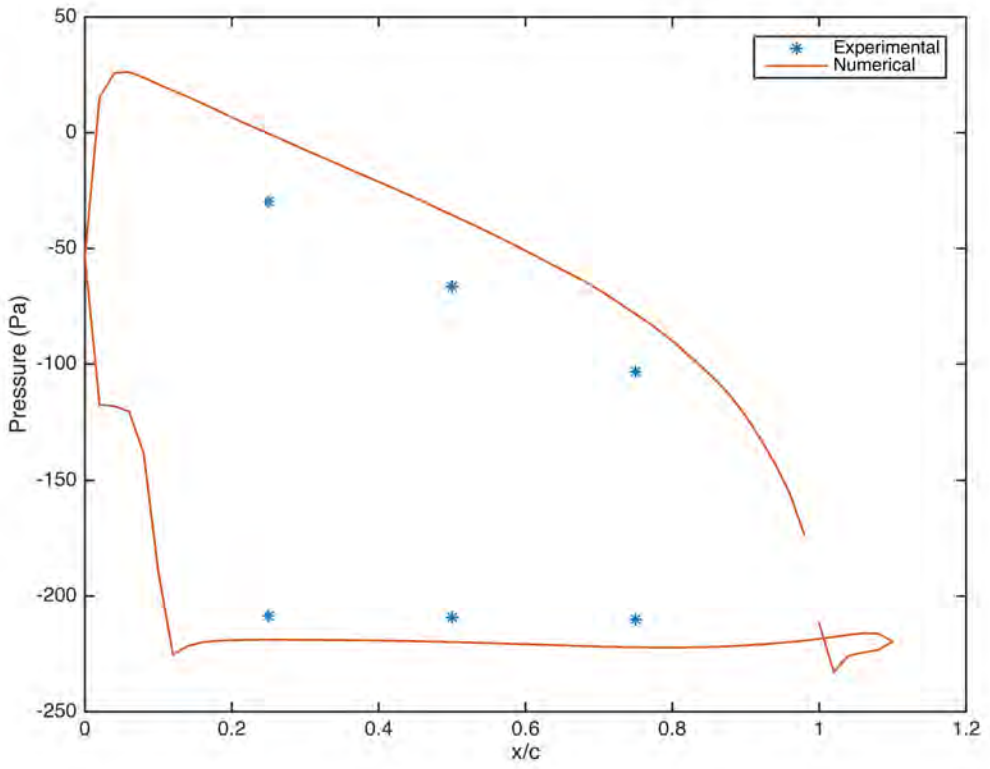

Figure 6.9: Relative static pressure for the first panel

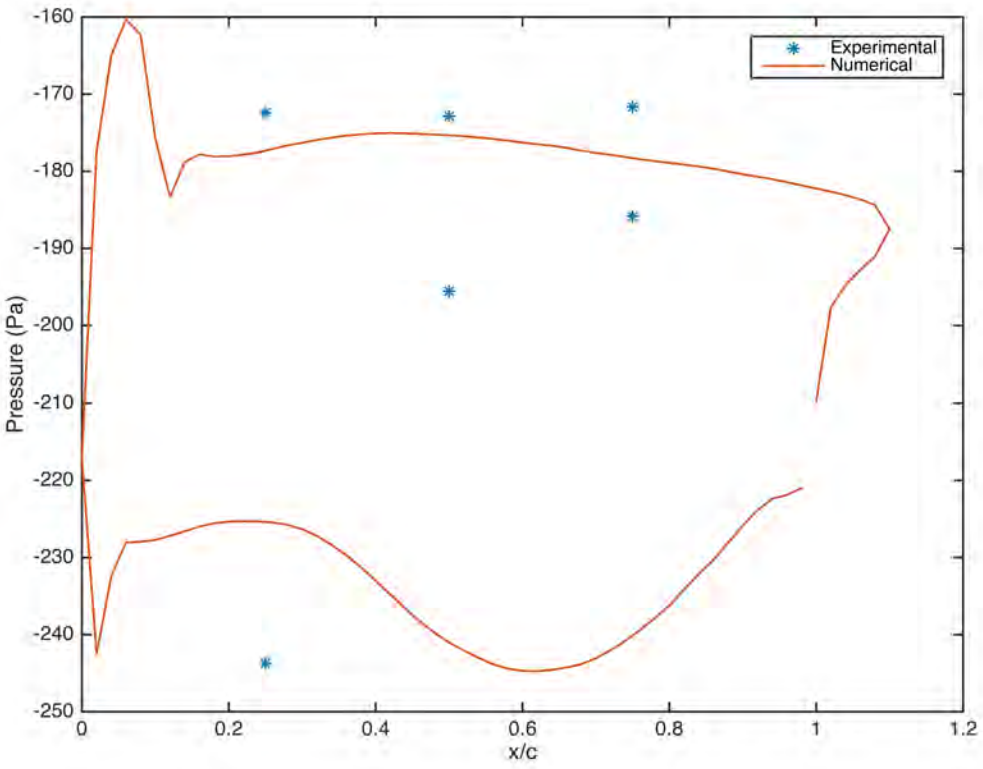

Figure 6.10: Relative static pressure for the second panel

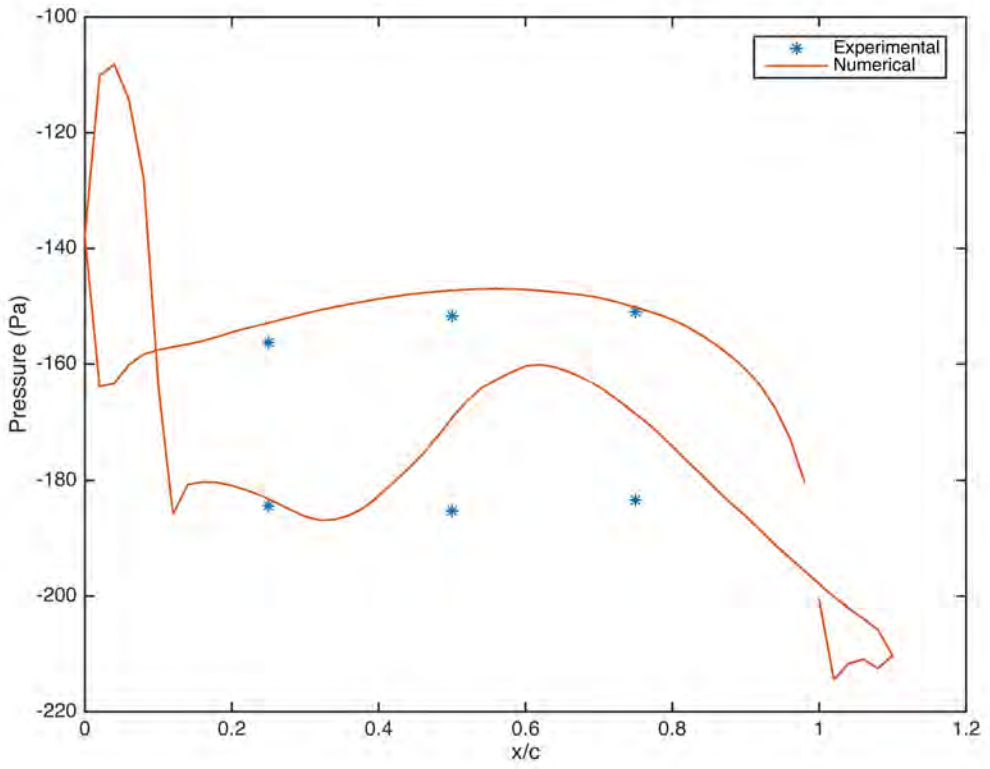

Figure 6.11: Relative static pressure for the third panel

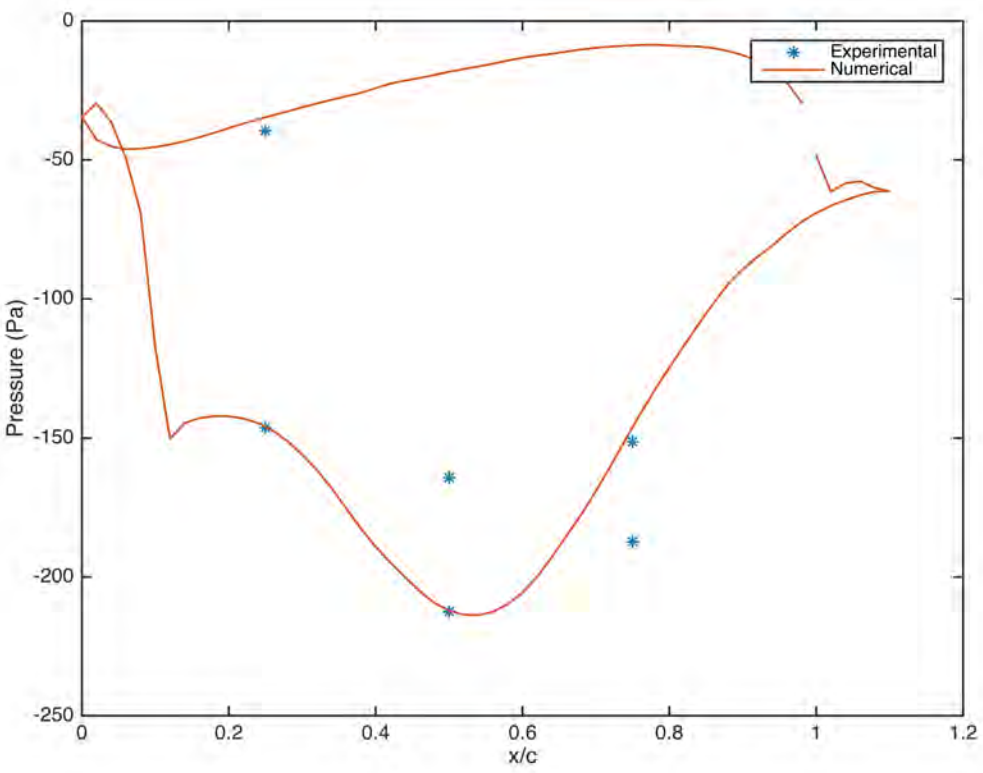

Figure 6.12: Relative static pressure for the fourth panel

Chapter 7

Conclusions

The purpose of the project is to validate a RANS model working with separated flows. To produce these separated flows, a configuration of 4 solar panels has been chosen. The RANS model to validate is the transition SST model.

The accuracy of the experimental data has to be evaluated by separating the different shooting frames. The two first shootings, which cover the region before the first panel and the region between the first and the second panel, have a very good quality. The shooting between the second and the third panel is still having a good quality, but the measurements taken in the fourth shooting are not reliable. The position where the laser is located, and the fact that the fourth panel is near a conflictive zone, do not help to avoid reflections that can produce inaccurate results. Anyway, PIV image can be said to have quite good quality. The main problem is the presence of the seeding that 1) tends to evaporate quickly at high speed, 2) in the wake could have lower density by itself.

Taking into account what have been said in the previous paragraph, the comparison between the experimental and the numerical results has to be done by parts. It has been easy to see that, between the front of the first panel and even the second panels, the numerical simulation is consistent with the experimental results. However, the comparison of the region after the fourth panel does not produce the expected result. The experimental result shows two turbulent wakes, while the numerical result only shows one. It has not been possible to analyse the region between the second and the third panel, breaking the continuity of the experimental results. Make the PIV in this region would be a great hint to study what occurs there in order to know why the experimental and the numerical results do not match. Another explanation for the mismatch between the results is that the numerical simulation does not end to converge, but gets stabilised jumping between two solutions. Due to this, URANS model would be more suitable to study the separated flow produced by the panel.

The comparison between the pressure taps and the FLUENT measurements are good in the first and third panel, but not in the second and fourth. This mismatch between the experimental and the numerical results may be due to the tubes contamination, but this cannot be asserted without more experiments. Furthermore, both results show that the maximum relative static pressure occurs at the front side in the first, second and fourth panel, but the third panel show the largest peak in the bottom of the back side in the numerical simulation.

It can be concluded that the RANS model works perfectly for the first separated flow, but it is necessary more experiments in order to know if it produces results at the separated flows of the last panels.

Chapter 8

Further considerations

With the experience acquired after making the project, certain changes can be defined, in both the experimental and the numerical parts, to improve the accuracy of results of the experiment, as well as reduce project costs. These savings can be used to realise more complicated experiments.

8.1 Experiment improvements

- Realise study cases with different free stream velocities.
- Use a different material to build the panels. The new material should reflect less light than the reflected by the actual black-painted powder. This will allow to remove the masks from the results, providing a larger zone to compare with the numerical results.
- Use a tomographic 3D PIV, which allows to record the U_w velocity and to visualise the flow from other perspectives.
- Use a splitter plate with a movable trailing edge.
- Use a hot-wire anemometer to measure the turbulence intensity, setting perfectly plane flow on the top side of the plate, because the PIV method does not give the best measurement. On one side, there is noise added up on the turbulence fluctuations, which produces a overestimating of the turbulence intensity. On the other hand, the PIV algorithm filters out everything that is smaller than the interrogation window, leading to an underestimated turbulence intensity.
- Add a grid panel to the wind tunnel to rack the turbulences created by the seeding, as it is explained in Section 4.2.6.
- Due to the structure of the wind tunnel, the laser source cannot be placed such that allows to record the section between the third and the fourth panel. This can be solved designing a new supporting structure for the laser or realising the experiments in a different tunnel with more space. Furthermore, a larger wind tunnel has a larger test section, which allows to make the experiments with more solar panel arrays and even setting a yawing angle of the panels with respect to the free stream direction.

8.2 CFD simulation improvements (FLUENT)

- Refine the mesh to obtain more accurate results. Furthermore, it is a key aspect in order to save time and money.
- Design the FLUENT case in 3D, implementing the geometry of the panels as they have been designed and built. This allows to see if the vortices that may appear in the panel laterals have any effects.

- Including in the wall boundary condition the roughness of the panels and tunnel walls to adapt the viscous behaviour to the reality.
- Change the FLUENT case from steady to transient.

Appendix A

Planes

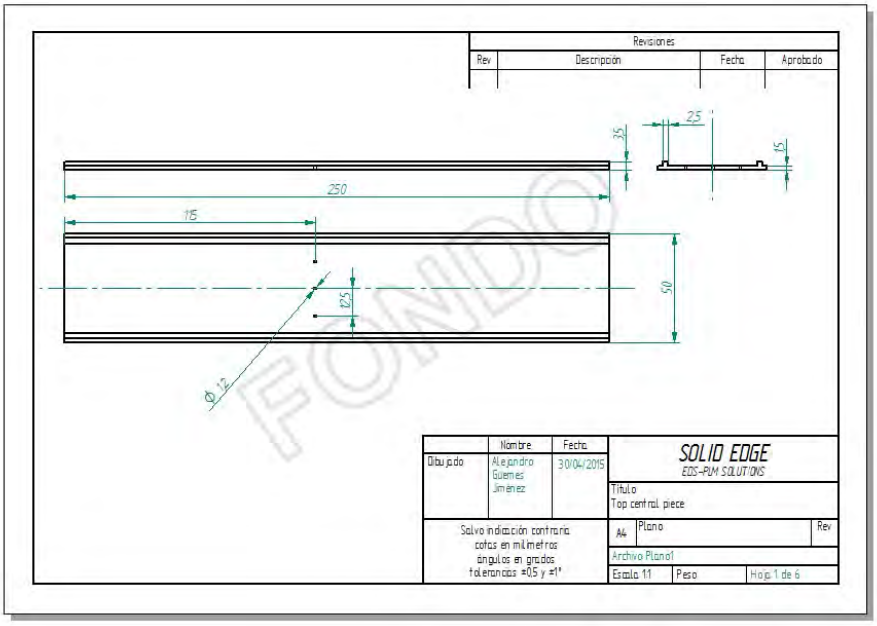

Figure A.1: Top central panel

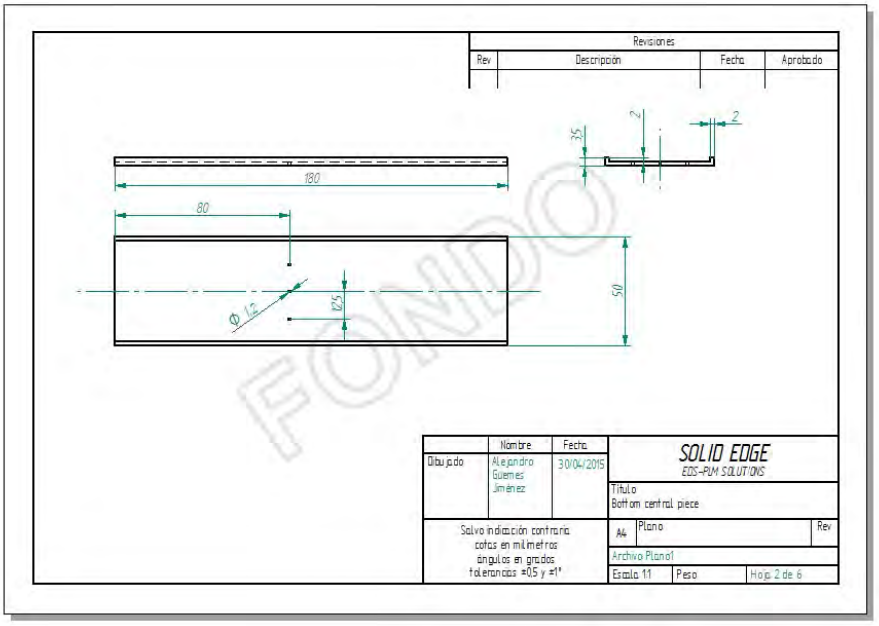

Figure A.2: Bottom central panel

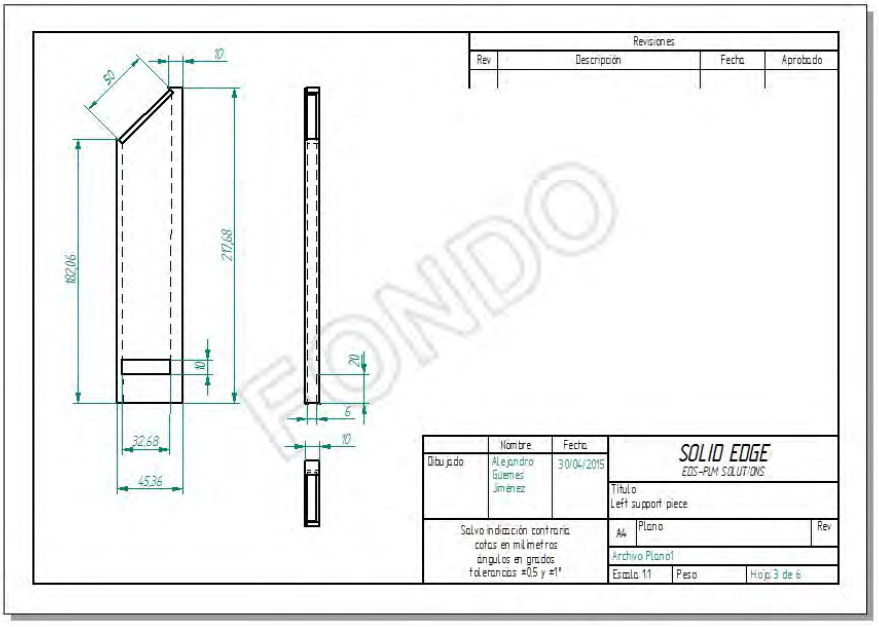

Figure A.3: Left support

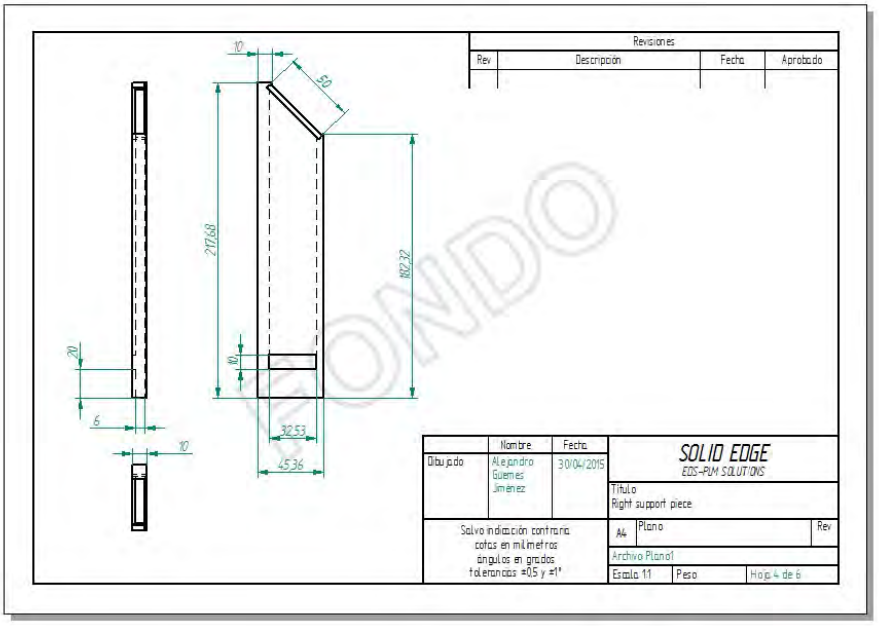

Figure A.4: Right support

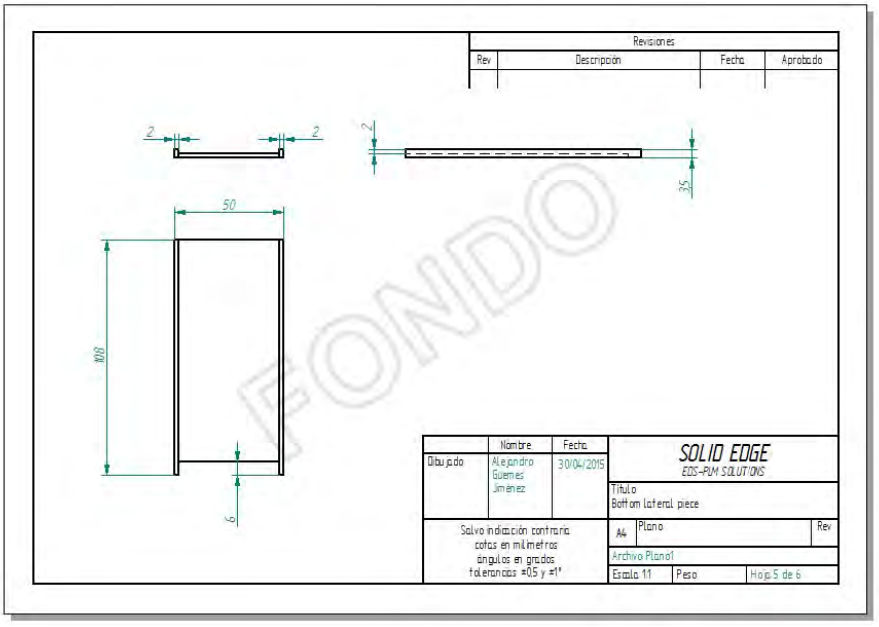

Figure A.5: Bottom lateral panel

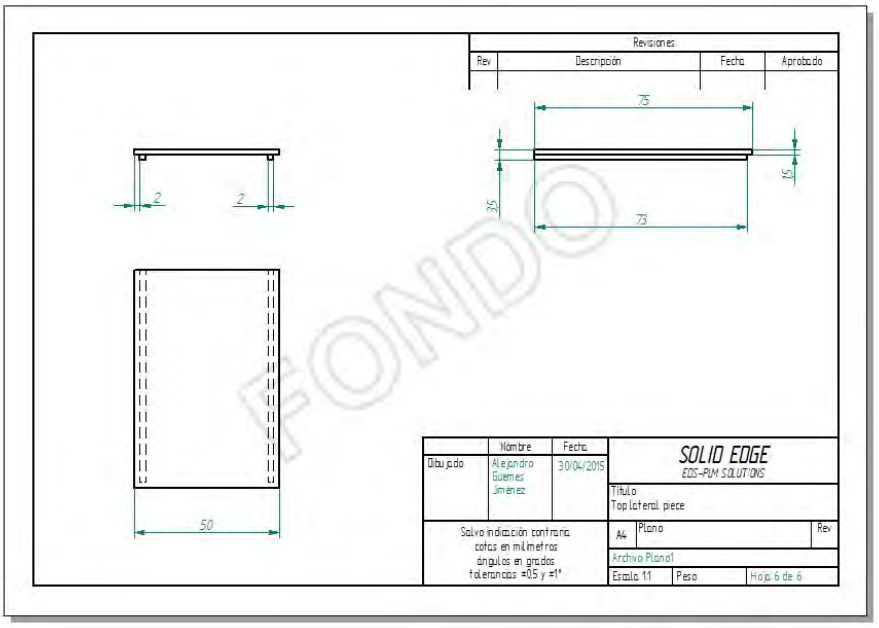

Figure A.6: Top lateral panel

Appendix B

Budget

The budget keeps an economic control over the project, so as a tool to locate potential sources of savings for future projects that attempt to reproduce the results of the experiment or for projects that seek to implement best mentioned in Section 8.1.

The wind tunnel rental price that appears in Table B.1 is an estimation, because the wind tunnel is not a rented equipment but property of the university. Its purchase price is 100000€, and it is suppose to have a lifespan of ten years, so renting the wind tunnel cost 10000€ per year. Each year is assumed to have 250 working days of 8 hours, leaving us with a rental price of 5€ per hour.

Working prices	
Labour cost (€/h)	20
Electric cost (€/kWh)	0.13
Wind tunnel rental price (€/h)	5

Table B.1: Working prices

Working time (h)	
Research time	10
Model design	12
Model manufacturing	16
Experimental part	120
Post-processing results	50
Numerical part	30
Thesis writing	100
TOTAL	338

Table B.2: Working time

Raw material (€)	
Cyanoacrylate	20
3D printer powder	200
Plastic tubes	10
Split plate	10
Seeding	50
Paint	14
TOTAL	304

Table B.3: Raw material prices

The wind tunnel operation cost comes from the electric cost of Table B.1, the experimental hours of Table B.2, and the wind tunnel installed power of Table 4.1.

Final budget (€)	
Wind tunnel rental	600
Tools	200
Wind tunnel operation	3.9
Raw material	304
Labour	6760
Matlab academic license	500
Fluent academic license	500
TOTAL	8867.9

Table B.4: Final project budget

Bibliography

Capote, J., Alvear, D., Abreu, O., Lázaro, M., and Espina, P. (2008). Influencia del modelo de turbulencia y del refinamiento de la discretización espacial en la exactitud de las simulaciones computacionales de incendios.

CFDOnline (2006). Turbulence intensity. http://www.cfd-online.com/Wiki/Turbulence_intensity.

Chevalier, H. and Norton, D. (1979). Wind loads on solar collector panels and support structure. Technical report, Texas A and M Univ., College Station (USA). Dept. of Aerospace Engineering.

Chimney, M., Fajardo, P., López-Díez, J., and Roibás, E. (2012). Aerodynamic performance of a single axis solar array.

Fajardo, P. and Raiola, M. (2014). Experimental aerodynamic testing of a single axis solar array.

Guerrero-Lemus, R. and Martínez-Duart, J. (2012). *Renewable Energies and CO2: Cost Analysis, Environmental Impacts and Technological Trends- 2012 Edition*. Lecture Notes in Energy. Springer London.

Hosoya, N., Peterka, J., Gee, R., and Kearney, D. (2008). Wind tunnel tests of parabolic trough solar collectors. *National Renewable Energy Laboratory Subcontract Report NREL/SR-550-32282*.

Keane, R. D. and Adrian, R. J. (1992). Theory of cross-correlation analysis of piv images. *Applied scientific research*, 49(3):191–215.

Menter, F. R. (1993). Zonal two equation k-turbulence models for aerodynamic flows. *AIAA paper*, 2906:1993.

Menter, F. R. (1994). Two-equation eddy-viscosity turbulence models for engineering applications. *AIAA journal*, 32(8):1598–1605.

Menter, F. R., Langtry, R., Likki, S., Suzen, Y., Huang, P., and Völker, S. (2006). A correlation-based transition model using local variables—part i: model formulation. *Journal of turbomachinery*, 128(3):413–422.

Quadrio, M. (2012). The RANS equations. DIA, Politecnico di Milano.

Reynolds, O. (1883). An experimental investigation of the circumstances which determine whether the motion of water shall be direct or sinuous, and of the law of resistance in parallel channels. *Proceedings of the royal society of London*, 35(224-226):84–99.

Scarano, F. and Westerweel, J. (2008). Advanced methods for experimental fluid dynamics. part i: Fundamentals of particle image velocimetry. Technical report, Universitá degli Studi di Napoli "Federico II" (Italy). Facoltà di Ingegneria.

Shademan, M. and Hangan, H. (2010). Wind loading on solar panels at different azimuthal and inclination angles. In *5th International Symposium on Computational Wind Engineering (CWE2010), Chapel Hill, NC, USA*.

Xu, Z., Shi, P., and Gu, I. Y.-H. (2006). An eigenbackground subtraction method using recursive error compensation. In *Advances in Multimedia Information Processing-PCM 2006*, pages 779–787. Springer.